



Exploring long-time response to radiation damage in MgO

B.P. Uberuaga^{a,*}, R. Smith^b, A.R. Cleave^c, G. Henkelman^a,
R.W. Grimes^c, A.F. Voter^a, K.E. Sickafus^a

^a *Los Alamos National Laboratory, Mailstop B268, Los Alamos, NM 87545, USA*

^b *Department of Mathematical Sciences, Loughborough University, LE11 3TU, UK*

^c *Department of Materials, Prince Consort Road, Imperial College, London SW7 2BP, UK*

Abstract

Using a variety of computational modeling and simulation methods, we examine the production and long-time evolution of damage created in irradiated MgO. We find that the damage produced in low energy (order 1 keV) collision cascades typically consists of point defects and small defect clusters. Over long times, interstitials annihilate with vacancies and aggregate with other interstitials, forming larger clusters that exhibit surprising behavior. For example, a six-atom interstitial cluster is found to have extremely high mobility. The implications of highly-mobile large clusters are explored via a rate theory model and comparison to other materials. We conclude that successful modeling of radiation damage evolution in MgO requires explicit treatment of large interstitial clusters.

© 2004 Elsevier B.V. All rights reserved.

PACS: 61.72.Ji; 61.72.Cc; 61.80.Az; 61.82.Ms

Keywords: MgO; Radiation damage; Molecular dynamics; Accelerated molecular dynamics; Temperature accelerated dynamics; Molecular statics; Density functional theory; Interstitial clusters; Defect mobility

1. Introduction

Understanding radiation effects in materials is key to developing important technologies, many of which are related to nuclear energy production. Experiment and theory, including computer simulation, offer differing approaches to examining

radiation damage. Experiments typically probe meso- to macroscopic time and length scales, while atomistic modeling focuses on both small length (\sim nm) and time (\sim ns) scales. Bridging the gap between experiment and theory is an active field of research, with much of this activity centered on extending the length scales of atomistic simulations. However, just as important for connecting theory to experiment is extending the time scales accessible to simulation. In this work, we apply conventional molecular dynamics (MD) and temperature accelerated dynamics [1] (TAD) to probe

* Corresponding author. Tel.: +1 505 667 9105; fax: +1 505 665 3909/+1 505 667 8021.

E-mail address: blas@lanl.gov (B.P. Uberuaga).

the behavior of radiation damage over long-time scales in MgO, reaching simulation times of seconds and longer. We also use both molecular statics and density functional theory to validate the results of these dynamics methods. We find that defects in MgO exhibit surprising behavior that impacts the tolerance of MgO to radiation damage. Some of the results presented here have appeared previously [2,3].

In our research effort, we are interested in the behavior of oxides when exposed to radiation environments. Oxides are clearly technologically important materials: they are key components of nuclear fuel rods in fission reactors [4] and radio-frequency windows in fusion reactors [5], and are used as host materials for nuclear waste [6,7]. In this particular study, we examine the properties of MgO. MgO, having been the subject of numerous experimental and theoretical studies, is a well understood engineering ceramic for which good quality empirical potentials exist. In addition, MgO is a relatively simple oxide that is relatively easy to characterize. This makes it a good candidate for testing our computational methodologies.

Our computational procedure consists of four parts. We begin by examining the collisional phase of a cascade using MD. Energy is imparted to a primary knock-on atom (PKA). This energy is transferred to other atoms in the lattice, creating a thermal spike in the vicinity of the original PKA. After a short time, typically a few hundred fs, the damage caused by this thermal spike peaks and begins to settle, so that after a few ps, most of the damage has been removed and only a few isolated point defects remain. We take representative defect geometries found from these MD simulations as the starting point for TAD simulations. TAD, an accelerated dynamics method [8], allows us to follow the motion of these defects out to much longer times, typically ms to s or even longer, depending on the properties of the defect. Using molecular statics, we explore alternative geometries to verify that we have indeed found ground state structures for the various defects encountered in the dynamics simulations. Finally, we calculate key quantities with density functional theory to ensure that the results of our empirical potential calculation apply to MgO.

Combining the results of all four of these computational methods, we find an interesting picture for radiation damage response in MgO. The initial cascade produces a small number of point defects – both interstitials and vacancies – and small defect clusters. Vacancies are essentially immobile at room temperature, while interstitials are mobile, diffusing on the μs time scale. As these interstitials diffuse, they either annihilate with vacancies or aggregate with other interstitials, creating larger and larger interstitial clusters. Initially, cluster mobility decreases with size – di-interstitials diffuse on the ms time scale while tetra-interstitials are essentially immobile. However, hexa-interstitial clusters are surprisingly mobile. These clusters can form in a long-lived metastable structure that diffuse on the ns time scale, faster than any other species we have observed in the system. They in turn impact mass transport in MgO and thus affect how MgO behaves when irradiated.

2. Methodology

2.1. Potential

As mentioned, we use four different computational methods to examine radiation damage behavior in MgO. Three of these – the MD, TAD and molecular statics – depend on the choice of a good empirical potential for their success. We have used a standard Buckingham [9] plus electrostatics potential, originally parameterized by Lewis and Catlow [10]. For the cascade simulations, in which, because of the high energies involved, the distance between the atoms can become too small for accurate description by the Buckingham potential, we have added a screened Coulomb potential for small particle separation [11]. The electrostatic terms were computed with either standard Ewald techniques (TAD) or the fast multipole method [12] (MD).

2.2. Cell geometries

In the cascade simulations, we embedded the active region of the crystal in charge-neutral cubes with charge-neutral $\{100\}$ faces in which the outer

two layers were held fixed. The size of these cells was chosen to ensure that the cascades did not interact significantly with the cell boundaries. This resulted in cells of 4000 atoms for PKA energies of 400 eV and cells of up to 160,000 atoms for the higher energy cascades of 5 keV.

For the TAD simulations, periodic boundary conditions were employed in all simulations of charge-neutral defects (e.g. stoichiometric interstitial clusters). These cells contained 512 atoms, although tests on larger cells were done to verify that cell-cell interactions were not significant. For studies of the charged tri-interstitial defects, cells with free surfaces were used containing 1000 atoms, of which 216 were allowed to move.

Finally, the molecular statics simulations employed the Mott–Littleton approach [13] in which the system is partitioned into spherical concentric regions. The defect is placed in the interior region, of radius 12.1 Å (Region I), in which all atoms are allowed to move and relax. Region II, surrounding Region I and extending to infinity, responds to the defect as a dielectric continuum according to the Mott–Littleton approximation [13]. To ensure a smooth transition between Regions I and II, an interfacial Region IIa, of radius 32.9 Å, is introduced. Ion positions within Region IIa are allowed to vary, subject to forces determined via the Mott–Littleton approximation; however, the interaction energies between Region I and II ions are calculated explicitly. These calculations are carried out using the code CASCADE [14].

We find consistent results among these three very different approaches to describing MgO, suggesting that our results are not sensitive to the details of the chosen geometry.

2.3. Details of cascade simulations

The cascade simulations consisted of imparting a large amount of kinetic energy to a PKA. This energy was varied from 400 eV to 5 keV, an energy not atypical of the sub-cascades produced in a 300 keV Kr⁺ radiation experiment. Trajectories were evenly distributed between PKAs of both O and Mg atoms and were randomly distributed over a solid angle representative of the crystal symme-

try. All trajectories were run for 8 ps, long enough for the thermal spike caused by the initial collision to dissipate. A total of 20 trajectories were performed at 400 eV while 12 each were done for 2 and 5 keV.

2.4. Details of TAD

Temperature accelerated dynamics (TAD) was applied to representative defect structures found in the cascade simulations in order to follow the dynamics of these defects out to long times. TAD is one of a number of accelerated dynamics techniques that allow for the simulation of much longer time scales than conventional MD [15]. The TAD algorithm involves running MD at a high temperature T_{high} , typically much higher than the temperature of interest T_{low} (300 K for the simulations reported here). However, this is done in a way that constrains the dynamics to the current state of the system (referred to as basin constrained MD, BCMD). Events seen at the high temperature are characterized, using the nudged elastic band method (NEB) [16,17], and the times of those events are extrapolated, via the barrier height found with NEB, to T_{low} . The BCMD procedure is continued until the stopping criterion is met. This stopping criteria depends on two parameters – δ , the uncertainty of missing an event and v_{min} , an assumed minimum prefactor in the system. These two parameters thus control the accuracy of a TAD simulation. Once the stopping time has been reached, the event occurring earliest at T_{low} is then accepted and the entire process repeated in the new state. The extrapolation of event times from T_{high} to T_{low} is exact if harmonic transition state theory holds for the system being studied at both temperatures.

In order to determine when an event has occurred, it must first be detected. In these simulations, an event was declared if, upon minimization, any atom had moved more than 0.25 Å from its position in the minimum of the current state.

In MgO, we find that the barriers for different defects to diffuse vary greatly, ranging from 0.3 to over 2 eV. To enhance the speed of the TAD simulations, we have employed a recently developed extension to TAD that incorporates the

dimer method [18]. This so-called dimer-TAD algorithm [19] uses the dimer method to find the minimum barrier to leave the state. This minimum barrier is then used to redefine the time at which the BCMD can be stopped, often reducing it dramatically. This new stopping criteria no longer depends on δ and v_{\min} . Instead, it depends on the minimum barrier in the system. This new TAD algorithm also allows us to tune T_{high} for the current state based on the minimum barrier, resulting in typical values between 300 K and 2000 K for MgO. In this study, we performed ten dimer searches per state, focused on the “active” region of the system, or that part of the system in which interstitials or vacancies resided.

2.5. Density functional theory

For the density functional theory (DFT) calculations, we employed the VASP code [20] with the PW91 functional and the projector augmented wave method [21] on supercells containing 216 lattice atoms and a plane wave basis with energies up to 400 eV. We determined that a single Γ -point sampling of k -space was sufficient to converge energies for this cell size. Increasing the k -point mesh to $2 \times 2 \times 2$ changed barrier heights by less than 0.001 eV.

3. Results

3.1. Structure of MgO

The structure of MgO is shown in Fig. 1(a). MgO, as all rock-salt structured compounds, belongs to the space group Fm $\bar{3}$ m. It consists of two interpenetrating tetrahedra in which O atoms are placed on the corners of one tetrahedron, in the 4a Wyckoff sites, and Mg atoms are in the corners of the other tetrahedron on 4b sites. The interstices of this structure lie in the center of this octant of the unit cell, or on the 8c sites. Fig. 1(b) shows the structure of the simplest Frenkel pair for this system in which one of the atoms is removed and placed in the 8c site. In MgO, this particular configuration of the Frenkel pair is not stable.

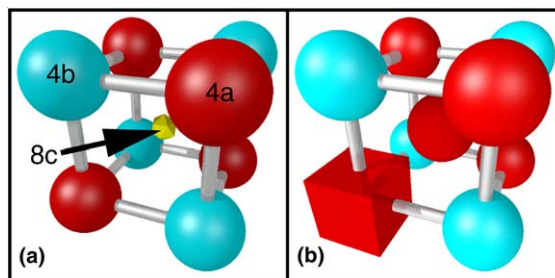


Fig. 1. (a) The basic structure of the MgO crystal. O atoms (dark/red color¹) occupy the 4a Wyckoff sites while Mg atoms (light/blue color) occupy the 4b Wyckoff sites of the two interpenetrating tetrahedra. The interstice site lies in the middle of this repeating unit, in the 8c site (represented by the octahedron). (b) Structure of the most elementary Frenkel pair, in which one of the atoms is removed from a lattice site (represented by the cube) and placed in the 8c site. In MgO, this particular structure is not stable. The Frenkel pair must be separated by 4 nearest neighbors before it is stable.

3.2. Initial defect production from cascades

The initial damage produced in an irradiated material is created via the collisions of high energy particles with atoms in the lattice of the material. Fig. 2 shows a typical 400 eV collision cascade in MgO. At $t = 0$, the initial knock-on event occurs. The damage quickly saturates ($t = 80$ fs) and settles ($t = 260$ fs), after which only a few isolated defects remain. In this simulation, the final defects consist of two vacancies and two interstitials, one of each type (Fig. 2(b)). Due to the strong electrostatic attraction between the oppositely charged interstitials, they move toward one another and by $t = 6.5$ ps they have combined to form an MgO di-interstitial (Fig. 2(c)).

Fig. 3 illustrates a second 400 eV cascade. As in Fig. 2, after the initial cascade has settled, a Mg interstitial is situated one lattice spacing from a Mg vacancy. In contrast to Fig. 2, in which the Mg interstitial combines with an O interstitial to form a stable di-interstitial, in Fig. 3, the O interstitial hops toward the Mg interstitial to form a di-interstitial which is still very close to the original Mg and O vacancies and soon annihilates with

¹ For interpretation of color in figures, the reader is referred to the web version of this article.

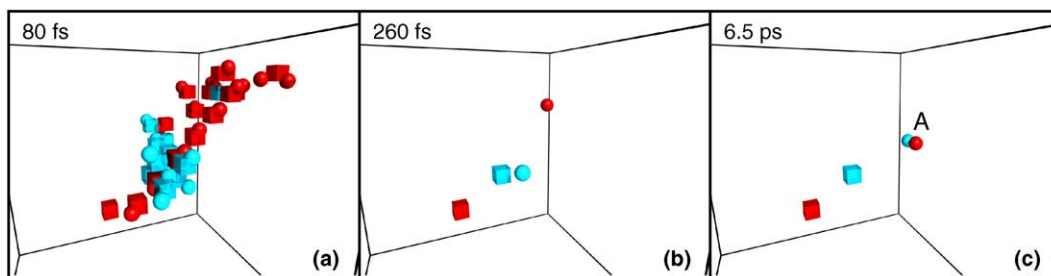


Fig. 2. The defects in a 400 eV cascade. The color scheme, used in this and all subsequent figures, is dark (red) for O defects and light (blue) for Mg defects. Spheres indicate interstitials, or atoms more than 0.8 \AA from a lattice site, and cubes indicate vacancies, or lattice sites with no atom within 0.8 \AA . (a) At $t = 80 \text{ fs}$, the number of displaced atoms saturates. (b) By $t = 260 \text{ fs}$, most of the defects have recombined, leaving only a few isolated defects. (c) By $t = 6.5 \text{ ps}$, the interstitials have formed a di-interstitial (labeled A).

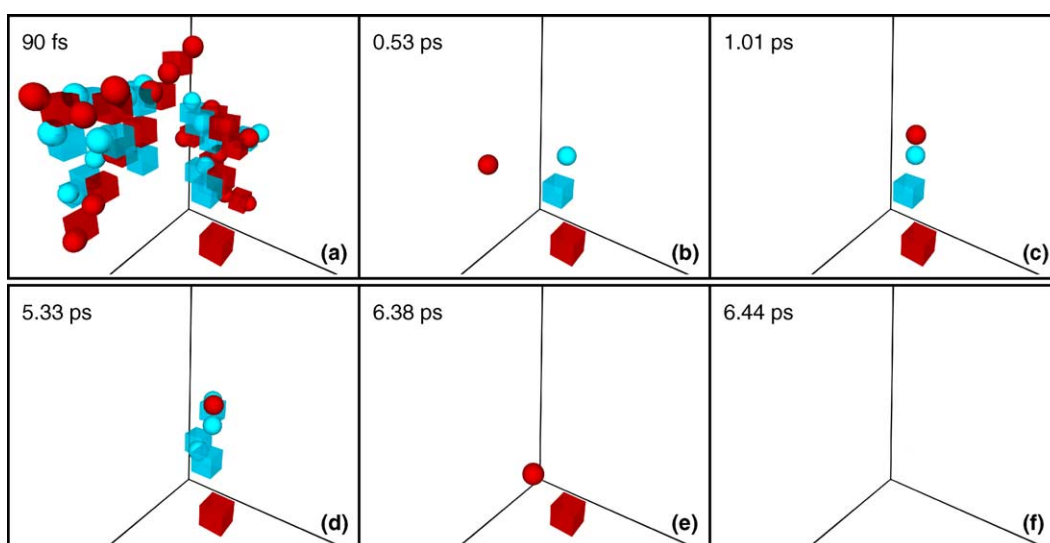


Fig. 3. Recombination events in a cascade generated by a 400 eV PKA in MgO. (a) The number of displacements peaks at 90 fs. (b) By 526 fs, most of the defects have recombined. At this stage the Mg interstitial is only 1 lattice unit from the Mg vacancy. (c) After 1006 fs, an MgO di-interstitial forms. (d) The Mg atom in the di-interstitial recombines with the nearby vacancy after 5327 fs. (e) The remaining O atom hops closer to the remaining O vacancy after 6376 fs. (f) The final event leading to complete recombination occurs after 6437 fs.

them. Whether interstitial defects annihilate with vacancies, as shown in Fig. 3, or aggregate with other interstitials (Fig. 2) depends on the complex electric field created by all of the defects in the vicinity.

From these simulations, we observe that the main mechanism for interstitial migration is to move between 8c sites (see Fig. 1(a)) in the $\langle 111 \rangle$ direction via a collinear interstitialcy mechanism, in agreement with the prediction of Ref. [22].

In general, only a small number of point defects, both interstitials and vacancies, are produced in the 400 eV cascades. In over half of the 20 trajectories run at 400 eV, the crystal completely reformed, leaving no residual damage after 8 ps of simulation time. In the rest, in addition to point defects, a few small clusters, specifically di-interstitials and di-vacancies, formed. However, the numbers of these were small: in all 20 simulations, 3 di-interstitials and one di-vacancy were formed.

Table 1

The total number of Frenkel pairs and principal defect types (mono- and di-interstitials and mono- and di-vacancies) for PKA energies of 0.4, 2 and 5 keV remaining after the collisional phase ($t = 8$ ps) of a cascade

PKA energy (keV)	Number of trajectories	Number of defects					
		Frenkel pairs	Mono-int O/Mg	Mono-vac O/Mg	Di-int	Di-vac	Perfect lattice
0.4	20	10	3/1	5/3	3	1	13
2	12	84	21/24	33/30	15	6	0
5	12	216	57/62	78/80	39	15	0

In addition, one tri-interstitial formed at 2 keV and 4 tri-interstitials, one tetra-interstitial and one 7-interstitial cluster formed at 5 keV. This table originally appeared in [2].

The total number of each principal defect formed in the 400 eV as well as higher energy cascades is summarized in Table 1.

As illustrated in Table 1 and Figs. 4 and 5, as the PKA energy is increased, the total number of defects and the number of larger defect clusters increases as well. In addition, the defects tend to be separated by larger distances than in the 400 eV cascades. As in the 400 eV simulations, di-interstitials tend to form not directly during the cascades, but rather as the result of migration processes during the tail end of the cascade. This illustrates the need to explore the behavior of these defects to even longer times, as it is over these longer times that important processes such as aggregation occur.

3.3. Long-time behavior of defects

Using MD, the collision cascade simulations are able to observe the creation and subsequent kinetics of the radiation-induced damage out to about 10 ps. As seen in those simulations, aggrega-

tion and annihilation of residual defects occurs after the thermal spike has settled and involves activated thermal events. Using TAD, we follow the behavior of these defects out to long times in which further annihilation and aggregation occurs, leading to the formation of structures with surprising properties.

Fig. 6 shows a TAD simulation of the annealing at 300 K of typical damage resulting from a 400 eV collision cascade. The initial configuration, consisting of two isolated vacancies and a di-interstitial, is very similar to that seen in Fig. 2(c). At 300 K, the vacancies never move during the length of the simulation. An isolated MgO di-interstitial, moving primarily in $\langle 111 \rangle$ directions via a collinear interstitialcy mechanism very similar to that of an isolated interstitial, diffuses on the time scale of tenths of seconds with a barrier of 0.75 eV. However, in the presence of the vacancies, because of the strong electrostatic interactions, this barrier is reduced so that by $t = 0.08$ s, the di-interstitial reaches the O vacancy and partly annihilates with the vacancy. The remaining Mg interstitial quickly

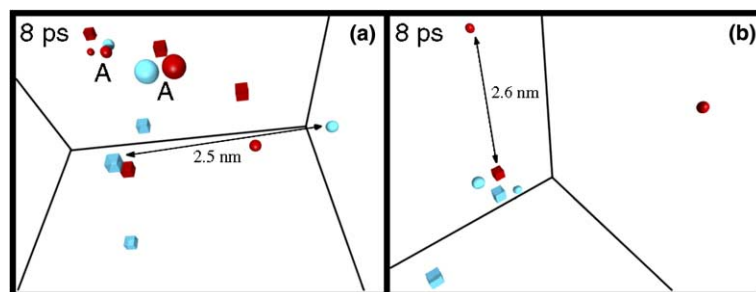


Fig. 4. Examples of the spread-out residual damage after the collisional phase of the cascade at 2 keV. (a) The image shows 3 separated Mg vacancies and 4 O vacancies. There are 2 MgO di-interstitials (labeled A), 1 Mg interstitial and 1 O interstitial. (b) In a second case, only well-separated isolated interstitials and vacancies occur.

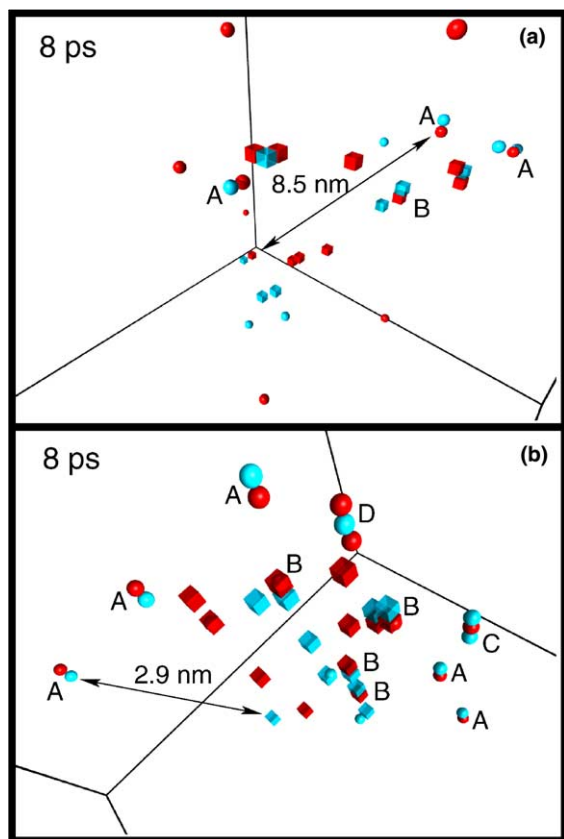


Fig. 5. Typical defects remaining after a 5 keV cascade. (a) The image shows 3 MgO di-interstitials and 2 di-vacancies in addition to isolated interstitials and vacancies. The length of the cube box side shown for perspective purposes is 11.9 nm. (b) In this case the cascade is more compact. There are 3 di-vacancies in addition to 5 di-interstitials, 2 tri-interstitials, 3 O interstitials and 1 Mg interstitial. The distance between the two tri-interstitials is 1.9 nm. Defects are labeled as (A) di-interstitials, (B) di-vacancies, (C) Mg–O–Mg tri-interstitials and (D) O–Mg–O tri-interstitials.

finds the Mg vacancy, completing the annealing process and healing the crystal.

Similar simulations were performed in order to watch the aggregation and subsequent migration of larger clusters. We can summarize the key behavior by quoting the migration barrier for these defects to diffuse. The diffusion barriers for isolated interstitials, found with molecular statics (see below), are 0.32 eV for the Mg interstitial and 0.40 eV for the O interstitial. For di-interstitials, we find a diffusion barrier of 0.75 eV. Tri-

interstitials diffuse with a very similar barrier: 0.79 eV for the Mg–O–Mg structure and 0.80 eV for the O–Mg–O tri-interstitial. The barrier for tetra-interstitials to diffuse is even higher – 1.68 eV – which means that they are essentially immobile at room temperature.

From these results, we begin to see a trend of decreasing mobility with increasing interstitial cluster size. The fact that clusters of size four are immobile suggests that these might be the nucleus of interstitial dislocation loops. However, TAD simulations reveal that the mobility of even larger clusters behaves more like isolated interstitials than like tetra-interstitials. Fig. 7 shows a TAD simulation of a system containing a di- and tetra-interstitial. Because of the immobility of the tetra-interstitial, the beginning of the simulation is dominated by the diffusion of the di-interstitial. Once they meet, they form a six-atom interstitial cluster that diffuses very quickly. The diffusion barrier of this geometry of the hexa-interstitial is only 0.24 eV, lower than even that for the isolated interstitials. This cluster's diffusion is characterized by one-dimensional motion, with the cluster confined to move in one of the $\langle 110 \rangle$ directions in the crystal.

Further exploration has revealed that the hexa-interstitial found via the TAD simulation of Fig. 7 is not the ground state structure of the hexa-interstitial. However, the lifetime of this metastable state is very long. The smallest barrier we have found for decay from the metastable to ground state hexa-interstitial is about 1.3 eV, meaning that the metastable hexa-interstitial will last for years at room temperature. We also find that the ground state hexa-interstitial is more mobile than the tetra-interstitial. It diffuses with a barrier of 1.04 eV, hopping about once every 100 s at room temperature. This is a relatively short-time scale compared to many experimental conditions and the hexa-interstitial will likely be an important species governing mass transport in MgO.

The octa-interstitial behaves in a qualitatively similar manner to the hexa-interstitial. A metastable form exists that diffuses with a barrier of 0.66 eV. The barrier to decay to the ground state octa-interstitial is 1.52 eV. The ground state

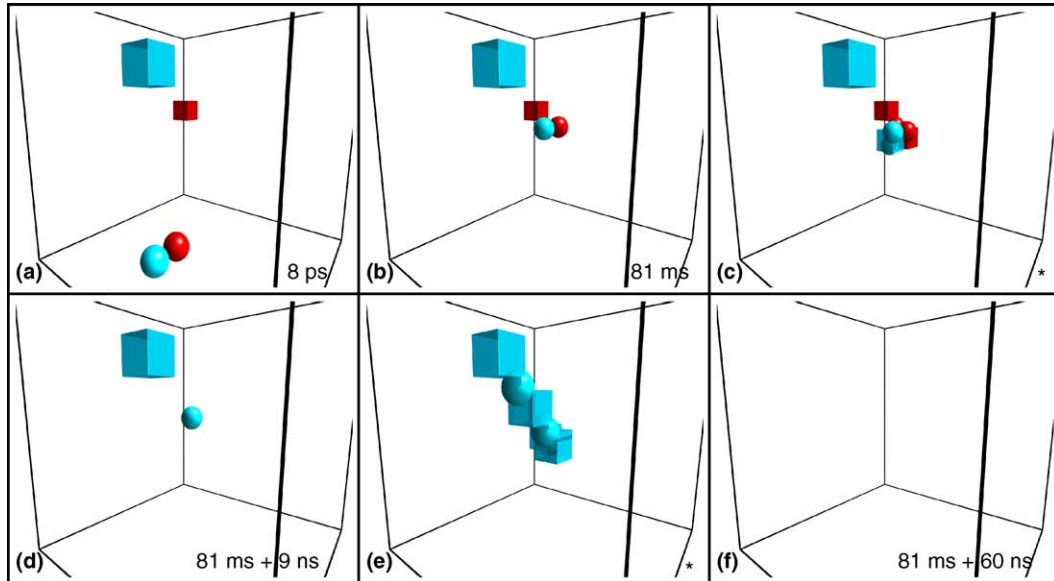


Fig. 6. A typical TAD simulation. (a) The initial configuration contains a di-interstitial and two vacancies, similar to the final state of Fig. 2(c). (b) After $t = 0.081$ s, the di-interstitial has diffused toward the O vacancy. (c) 9 ns later, via a concerted event involving several atoms, (d) the O atom of the di-interstitial annihilates the O vacancy. (e) The remaining Mg interstitial then quickly recombines with the Mg vacancy via a long-range, concerted mechanism involving many atoms (f) which results in the reformation of the perfect crystal 51 ns after the first annihilation event. The * indicates structures interpolated between states from before and after the event.

structure is again essentially immobile at room temperature, diffusing with a barrier of 1.7 eV.

All of the TAD simulations are summarized in Fig. 8 in the form of the both the barriers for diffusion versus interstitial cluster size and the corresponding diffusion time scale at room temperature.

3.4. Stability of defects

Using molecular statics [23], we analyzed the stability of interstitials clusters versus cluster size. These results are summarized in Fig. 9. It is clear that interstitial clusters become more stable with size, with di-interstitials bound by about 3.49 eV per atom to ten-atom interstitial clusters being bound by just over 5 eV per atom. The binding energy per atom begins to plateau with about 10 atoms per cluster. However, over 10 eV worth of energy is gained in the system for each MgO unit added to the cluster, suggesting that there is no energetic limit on the size of clusters. This coincides with the experimental observation of large interstitial dislocation loops forming in MgO.

As mentioned previously, the isolated interstitial of both types (O and Mg) prefers to sit at the 8c site (see Fig. 1(b)). It diffuses by a collinear interstitialcy mechanism in which the interstitial in one 8c site replaces a lattice atom which simultaneously moves to another 8c site, with both atoms moving along the same $\langle 111 \rangle$ direction. The barriers for interstitial diffusion are 0.32 eV for Mg and 0.40 eV for O.

The larger interstitial structures represented in Fig. 9 were constructed by examining the structure of the ground state hexa- and octa-interstitials found in the TAD simulations, shown in Fig. 10. By comparing the two structures, a common motif is found in which the structure of the octa-interstitial (Fig. 10(b)) can be viewed as two hexa-interstitials of Fig. 10(a) centered in neighboring 8c sites, with overlapping atoms removed. This motif was extended to build the larger interstitial clusters whose energies are given in Fig. 9. We cannot be certain at this point that these are the most stable geometries for these cluster sizes, but they do illustrate the strong

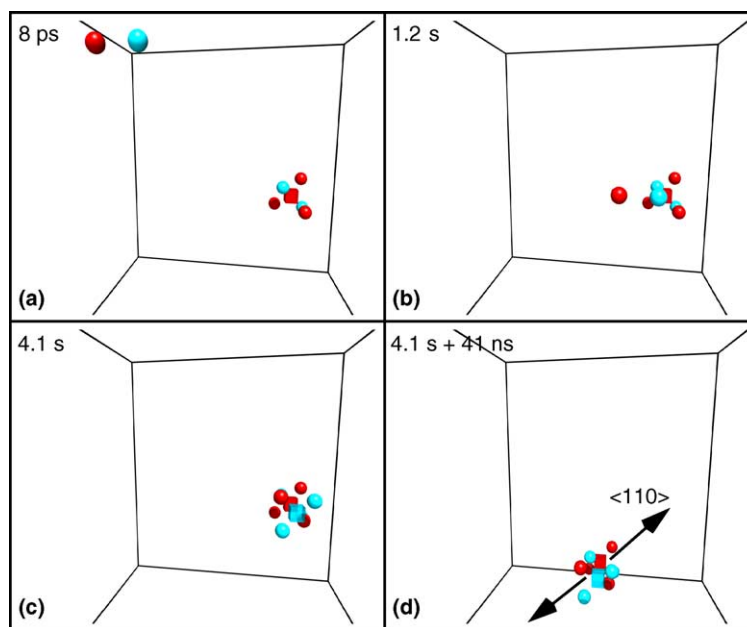


Fig. 7. TAD simulation of the formation of a hexa-interstitial at 300 K. (a) A di- and tetra-interstitial begin about 1.2 nm apart. (b) $t = 1.2$ s; the di-interstitial has approached the immobile tetra-interstitial. (c) By $t = 4.1$ s, the combined cluster has annealed to form the metastable hexa-interstitial; (d) this metastable form diffuses on the ns time scale with a barrier of 0.24 eV. The one-dimensional $\langle 110 \rangle$ diffusion direction is indicated.

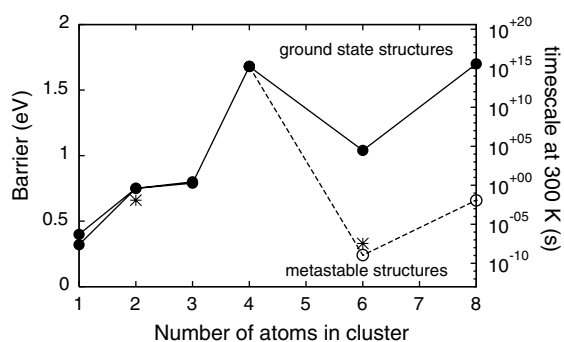


Fig. 8. Diffusion barriers for interstitial clusters versus cluster size. The time scale for diffusion at 300 K is also shown. The dashed line indicates barriers for metastable clusters. Stars indicate barriers calculated with DFT.

additional binding energy associated with larger clusters.

3.5. Validation of the empirical potential

Finally, density functional theory has been used to validate some of the key results found with the

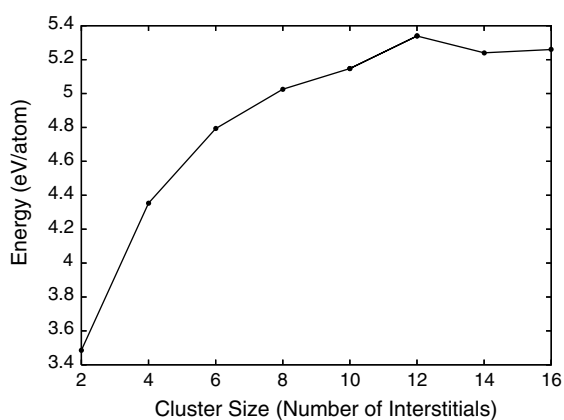


Fig. 9. Binding energy for interstitial clusters versus cluster size.

empirical potential, to ensure that the results we describe here do indeed apply to MgO. We calculated both the formation and migration energies for both the di- and metastable hexa-interstitials. We find formation energies for the di- and metastable hexa-interstitial of 12.8 and 31.1 eV, respec-

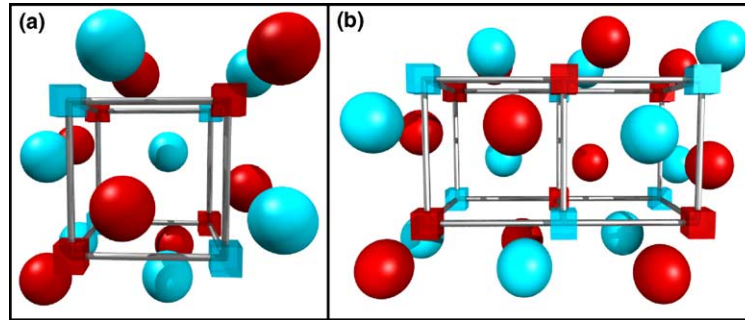


Fig. 10. Ground state structure of (a) the hexa-interstitial and (b) the octa-interstitial. The hexa-interstitial is centered around one MgO unit cell (the bars and vacant lattice sites, represented by cubes) while the octa-interstitial extends over two unit cells. Each of the bars connecting the vacant sites lies along a $\langle 100 \rangle$ direction. In the hexa-interstitial structure, six atoms have been inserted in the center of the basic MgO structural unit, displacing the crystallographic atoms away from their lattice sites. The octa-interstitial exhibits a similar structure in which eight atoms have been inserted in the center of two MgO structural units.

tively. These agree well with the empirical potential values of 11.9 and 28.5 eV, especially in the context of the high energies involved in the collision cascades. The agreement between the diffusion barriers is remarkable: 0.66 and 0.33 eV with DFT versus 0.75 and 0.24 eV with the empirical potential (see Fig. 8).

We have further analyzed the DFT results by calculating the Bader charges [24,25] associated with the atoms in and around the metastable hexa-interstitial cluster. The results of this analysis are shown in Fig. 11 as the net charge transferred

to or from each atom. In the bulk, we find that the amount of charge transferred is nearly the full formal charge assumed by the model: each Mg atom transfers 1.72 electrons to each O atom. The amount of charge transferred among those atoms composing the metastable hexa-interstitial is slightly less, with the least amount transferred in the system being 1.64 electrons. The amount of charge transferred among the atoms in the defect and those in the bulk is similar, possibly explaining why the ionic model does so well in describing these neutral bulk defects.

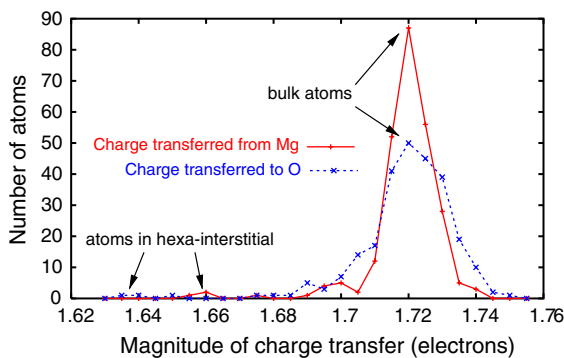


Fig. 11. Bader decomposition of the DFT charge transfer in and around the metastable hexa-interstitial cluster, relative to an isolated atom. In the bulk, each Mg atom has a net charge of 1.72 while each O atom has a net charge of -1.72 , illustrated by the peak in the charge transfer. The atoms in the metastable hexa-interstitial cluster, labeled in the figure, transfer slightly less charge than the bulk.

4. Discussion

Through a combination of a number of computational methodologies, we have uncovered an interesting picture for the room-temperature evolution of radiation damage in MgO on the atomic scale. Low-energy collision cascades produce a small number of point defects and small defect clusters. Vacancy defects are immobile at 300 K, while single interstitials of both types can diffuse quickly. They can thus either annihilate with vacancies or aggregate with other interstitials, forming larger interstitial clusters. These clusters are more stable with size, though their mobility appears uncorrelated with size. Di-interstitials are less mobile than isolated interstitials and tetra-interstitials are essentially immobile at room temperature conditions. However, the hexa-interstitial

can exist in a form that has a higher mobility than any other species we have observed in the system. These clusters, if they are created, will influence mass transport in the system and will likely impact predictions of the overall damage accumulation rate in MgO.

4.1. Impact of mobile large clusters

The most important question one can ask about these results is how relevant are these mobile large clusters? Will they impact any observable property of MgO? As an initial attempt to gauge the importance of including these species in higher level models of radiation damage in MgO, we have performed calculations using a chemical rate theory model of radiation damage evolution in MgO similar to that used by Yoshida and Kiritani [26]. This is a simplified model that excludes all information about the three-dimensional nature of the problem, but should give us a qualitative idea of the impact of including or excluding mobile hexa-interstitial clusters in such models.

The model includes a number of reactions, which are summarized here:

$$\frac{dC_v}{dt} = (1 - C_v)(1 - Z_1 C_v)P - Z_1 \sum_{n=1}^{n_{\max}} \Gamma_{i_n} C_v C_{i_n}, \quad (1)$$

$$\begin{aligned} \frac{dC_{i_n}}{dt} = & (1 - C_v)(1 - Z_1 C_v)P\delta_{n1} \\ & + Z_2 \sum_{p=1}^{n-1} \sum_{q \geq p}^{n-1} \delta_{n(p+q)} (\Gamma_{i_p} + \Gamma_{i_q}) C_{i_p} C_{i_q} \\ & - Z_3 \Gamma_{i_n} \sqrt{C_{iL} C_L} C_{i_n} - Z_1 \Gamma_{i_n} C_v C_{i_n} \\ & - Z_2 \sum_{p=1}^{p \leq n} (\Gamma_{i_n} + \Gamma_{i_p}) C_{i_n} C_{i_p}, \end{aligned} \quad (2)$$

$$\frac{dC_L}{dt} = Z_2 \sum_{p=1}^{n_{\max}} \sum_{q \geq p}^{n_{\max}} \Theta(p+q - n_{\max}) (\Gamma_{i_p} + \Gamma_{i_q}) C_{i_p} C_{i_q}, \quad (3)$$

$$\frac{dC_{iL}}{dt} = Z_3 \sum_{p=1}^{n_{\max}} p \Gamma_{i_p} \sqrt{C_{iL} C_L} C_{i_p} + A \frac{dC_L}{dt}. \quad (4)$$

In these equations, P is the damage production rate of both interstitials and vacancies (assumed to be always created in pairs). C_{i_n} is the concentration of interstitial clusters of size n , C_v is the concentration of vacancies, C_L is the concentration of interstitial dislocation loops, and C_{iL} is the concentration of interstitials in those loops. Γ_{i_n} is the hopping rate of interstitial clusters of size n . Z_1 is the capture volume of vacancies measured in terms of the number of atomic sites around the vacancy that can capture an interstitial species, Z_2 is that of interstitials capturing one another, and Z_3 is that of interstitial dislocation loops capturing interstitial clusters. These are assumed to be equal for all interactions and do not take into account differences in strength of Coulomb interaction between species. That is, the volume Z_1 for vacancies to capture both interstitials and hexa-interstitials is the same. There is a separate $\frac{dC_{i_n}}{dt}$ equation for each interstitial cluster size to be considered, up to $n = n_{\max}$. Anything larger than n_{\max} is considered an interstitial dislocation loop. A is the average number of interstitials put into loops when a new loop is formed. δ_{ij} is the Kronecker delta symbol, which is 1 if $i = j$ and 0 otherwise. $\Theta(x)$ is the Heaviside step function where $\Theta(x) = 0$ if $x < 0$ and $\Theta(x) = 1$ if $x \geq 0$.

Eq. (1) represents the creation, via P , and the annihilation, via encounters with interstitials, of vacancies. The concentration of interstitial clusters of size n is given by Eq. (2). Isolated interstitials (interstitial “clusters” of size $n = 1$) are created, along with vacancies, via the production rate P . An interstitial cluster of size n can partially annihilate with a vacancy and be reduced in size by one (effectively annihilating the cluster of size n and creating a cluster of size $n - 1$) via the recombination volume Z_1 . Two interstitial clusters can interact through the recombination volume Z_2 to create larger clusters of size n . They can also be absorbed by interstitial dislocation loops, through the recombination volume Z_3 , reducing the number of clusters but increasing the size (C_{iL}) of interstitial dislocation loops. New loops are created when two clusters meet to form “clusters” of size $n > n_{\max}$, the definition of a new interstitial dislocation loop. Eqs. (3) and (4) represent the creation of new loops and

the growth of existing loops via the capture of interstitial clusters.

In the case of MgO, because we are interested in room temperature, a temperature at which vacancies are immobile, we have included no mobility for vacancies and therefore no clustering mechanisms either. All vacancies are assumed to be isolated vacancies here. We have taken $\Gamma_{i_4} = 0$, as tetra-interstitials are also immobile at this temperature on experimental time scales. In addition, while we have not explicitly calculated any properties for the penta-interstitial, we assume here that it behaves like the tetra-interstitial and that $\Gamma_{i_5} = 0$. The non-zero rates were calculated using $\Gamma_{i_n} = v_{i_n} \exp(-E_{m,i_n}/k_B T)$, where E_{m,i_n} is the migration energy for clusters of size n . All rate prefactors v_{i_n} were set to $10^{13}/s$. For simplicity, we have also assumed that $Z_1 = Z_2 = Z_3 = 100$ atomic sites. We have assumed an initial production rate $P = 10^{-4}/s$. These values have not been carefully tuned to the properties of MgO, but at this point we are more interested in qualitative effects than quantitative results. Finally, we have not made any distinction between O and Mg in this model. That is, we are only modeling a single concentration of interstitials and vacancies. This seems reasonable as the results presented previously indicate that non-stoichiometric defects of differing types tend to behave very similarly. The diffusion barrier for isolated O interstitials is similar to that of Mg interstitials and here we have taken the average value, 0.36 eV, as the migration barrier for single interstitials. The same was done for tri-interstitials of both types: Mg–O–Mg and O–Mg–O. A is a parameter that is on the order of unity and is taken to be unity here. Finally, we consider clusters up to size $n_{\max} = 6$. These values are summarized in Table 2.

We find that most steady-state concentrations are unaffected by the presence of mobile hexa-interstitials. For example, the concentrations of vacancies C_v and interstitials in loops C_{iL} remain unchanged by including mobile hexa-interstitials. The time to reach steady-state is increased significantly when mobile hexa-interstitials are introduced into the system. The time for the vacancy concentration to reach steady-state at 300 K, for example, increases by over a factor of 3.

Table 2

Summary of the parameters used in the chemical rate theory model

Parameter	Value
P	$10^{-4}/s$
v_{i_n}	$10^{13}/s$
E_{m,i_1}	0.36 eV
E_{m,i_2}	0.75 eV
E_{m,i_3}	0.8 eV
E_{m,i_6}	0.24 eV
$\Gamma_{i_4}, \Gamma_{i_5}$	0
n_{\max}	6
Z_1, Z_2, Z_3	100
A	1

Where we do see a large impact of the mobility of the hexa-interstitial is in the concentration of loops C_L themselves and, correspondingly, their average size, estimated as the ratio C_{iL}/C_L and plotted in Fig. 12. By 300 K, the average size of interstitial dislocation loops is over an order of magnitude larger when mobile hexa-interstitials are included. Measuring the size of interstitial dislocation loops as a function of temperature may be an indirect way to experimentally probe the existence of large mobile clusters in MgO. We expect there may be orientation or shape effects as well, arising from the one-dimensional diffusion of the hexa-interstitial cluster, but exploring such effects will require more sophisticated models.

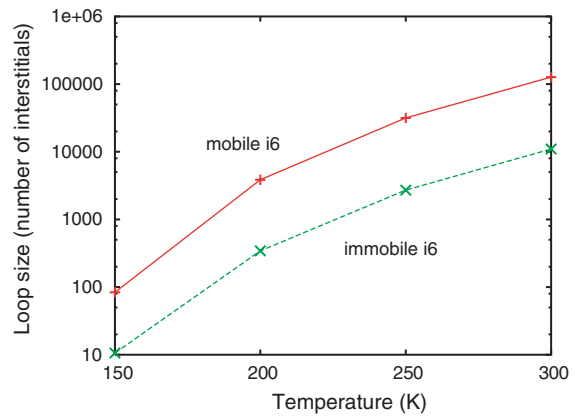


Fig. 12. Average size of interstitial dislocation loops in MgO, given as the number of interstitials in the loops, as a function of temperature for chemical rate theory models that do and do not include mobile metastable hexa-interstitials.

4.2. Iso-structural materials

It is also interesting to compare cluster mobility in MgO with iso-structural materials. Presumably, materials that are iso-structural to MgO would exhibit similar properties, though the details may differ. Both SrO and BaO have the same structure as MgO, but have a larger lattice constant, which possibly allows for greater mobility of defects because the material has, in a sense, a more open structure. That is what we observe. In Fig. 13, we compare the barriers for diffusion of the charge-neutral defects found in MgO with the diffusion barriers of the same defects in SrO and BaO, computed using the parameterizations for these materials reported in [10]. Vacancy clusters (not shown in Fig. 13) are still essentially immobile at room temperature. In general, interstitial cluster mobility in SrO and BaO is very similar. This is due to the fact that BaO is only about 7% bigger than SrO, while SrO is 23% bigger than MgO (as predicted by the empirical potentials we are using). The metastable hexa-interstitial is extremely mobile in SrO and BaO, hopping every ps. These would be very important species, even at low temperatures. On the other hand, tetra-interstitials are also much more mobile in SrO and BaO than in MgO, and thus could not be neglected in models

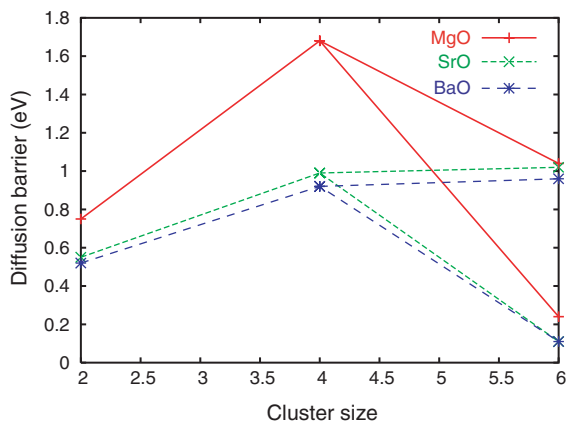


Fig. 13. The diffusion barrier versus cluster size for charge-neutral defects in SrO and BaO, materials that are iso-structural to MgO. Negative cluster sizes indicate vacancy clusters. The general trends in both materials are the same as in MgO, though mobility increases as the volume of the material increases.

of radiation damage in these materials at room temperature. At low temperatures, the only mobile species in SrO and BaO would be the hexa-interstitials, which would effectively be turned off in MgO at such temperatures. Probing the existence and relevance of mobile large clusters in these materials might be possible by comparing and contrasting the average loop size as a function of temperature.

5. Conclusion

Probing the long-time behavior of defects generated in collision cascades has revealed surprising behavior for larger interstitial clusters in MgO. A metastable form of the hexa-interstitial cluster, which can form when di- and a tetra-interstitial clusters meet, is the most mobile species encountered in this material. While it is currently difficult to directly measure the existence of these clusters experimentally, a simple model indicates that they will have an impact on the average size of dislocation loops. These defects are also present and important in iso-structural materials, such as SrO and BaO, and comparing and contrasting these materials might offer an approach whereby experiments can determine the existence and relevance of these larger mobile clusters. Further work is required to determine if other characteristics of these clusters – such as confinement of the diffusion of the metastable hexa-interstitial to one-dimension – might result in experimentally observable features in irradiated MgO.

Acknowledgements

We acknowledge helpful discussions with F. Montalenti, G. Pacchioni, J.H. Harding and D.J. Harris. This work was supported by the United States Department of Energy, Office of Science, Office of Basic Energy Sciences, Division of Materials Sciences and Engineering.

Note added in proof

After submission of this manuscript, we discovered that the migration barrier quoted for the tri-interstitial was not converged with respect to cell

size. A better converged value is 0.6eV, approximately 0.2eV lower than quoted above. However, we have verified that none of the results discussed in Section 4 are affected by this error. Future work will address this in more detail.

References

- [1] M.R. Sørensen, A.F. Voter, *J. Chem. Phys.* 112 (2000) 9599.
- [2] B.P. Uberuaga, R. Smith, A.R. Cleave, F. Montalenti, G. Henkelman, R.W. Grimes, A.F. Voter, K.E. Sickafus, *Phys. Rev. Lett.* 92 (2004) 115505.
- [3] B.P. Uberuaga, R. Smith, A.R. Cleave, G. Henkelman, R.W. Grimes, A.F. Voter, K.E. Sickafus, *Phys. Rev. B*, submitted for publication.
- [4] D.R. Olander, Fundamental aspects of nuclear reactor fuel elements, Technical Information Center, Office of Public Affairs, Energy Research and Development Administration, Springfield, Virginia, 1976.
- [5] C. Kinoshita, S.J. Zinkle, *J. Nucl. Mater.* 233–237 (1996) 100.
- [6] W.J. Weber, R.C. Ewing, C.R.A. Catlow, T.D. de la Rubia, L.W. Hobbs, C. Kinoshita, H. Matzke, A.T. Motta, M. Nastasi, E.K.H. Salje, E.R. Vance, S.J. Zinkle, *J. Mater. Res.* 13 (1998) 1434.
- [7] K.E. Sickafus, L. Minervini, R.W. Grimes, J.A. Valdez, M. Ishimaru, F. Li, K.J. McClellan, T. Hartmann, *Science* 289 (2000) 748.
- [8] A.F. Voter, F. Montalenti, T.C. Germann, *Annu. Rev. Mater. Sci.* 32 (2002) 321.
- [9] R.A. Buckingham, *Proc. R. Soc. London Ser. A, Math. Phys. Sci.* 168 (1938) 264.
- [10] G.V. Lewis, C.R.A. Catlow, *J. Phys. C: Solid State Phys.* 18 (1985) 1149.
- [11] J.F. Ziegler, J.P. Biersack, U. Littmark, *The Stopping and Range of Ions in Solids 1*, Pergamon, New York, 1985.
- [12] W.T. Rankin, J.J.A. Board, *Proceedings, 1995 IEEE Symposium on High Performance Distributed Computing*, 1995, p. 81.
- [13] N.F. Mott, M.J. Littleton, *Trans. Faraday Soc.* 34 (1932) 485.
- [14] M. Leslie, DL/SCI/TM31T. Tech. Rep., SERC Daresbury Laboratory, 1982.
- [15] F. Montalenti, M.R. Sørensen, A.F. Voter, *Phys. Rev. Lett.* 87 (2001) 126101.
- [16] G. Henkelman, B.P. Uberuaga, H. Jónsson, *J. Chem. Phys.* 113 (2000) 9901.
- [17] G. Henkelman, H. Jónsson, *J. Chem. Phys.* 113 (2000) 9978.
- [18] G. Henkelman, H. Jónsson, *J. Chem. Phys.* 111 (1999) 7010.
- [19] F. Montalenti, B.P. Uberuaga, G. Henkelman, A.F. Voter, in preparation.
- [20] G. Kresse, J. Hafner, *Phys. Rev. B* 47 (1993) 558; *Phys. Rev. B* 49 (1994) 14251; G. Kresse, J. Furthmüller, *Comput. Mater. Sci.* 6 (1996) 16; *Phys. Rev. B* 55 (1996) 11169.
- [21] G. Kresse, J. Joubert, *Phys. Rev. B* 59 (1999) 1758; P.E. Blöchl, *Phys. Rev. B* 50 (1994) 17953.
- [22] E.A. Kotomin, A.I. Popov, *Nucl. Instr. and Meth. B* 141 (1998) 1.
- [23] G. Busker, M.A. van Huis, R.W. Grimes, A. van Veen, *Nucl. Instr. and Meth. B* 171 (2000) 528.
- [24] R.F.W. Bader, *Atoms in Molecules – A Quantum Theory*, Oxford University Press, Oxford, 1990.
- [25] G. Henkelman, A. Arnaldsson, H. Jónsson, *Comput. Mater. Sci.*, submitted for publication.
- [26] N. Yoshida, M. Kiritani, *J. Phys. Soc. Jpn.* 35 (1973) 1418.